3D printing of hierarchically porous MOF monoliths using silica nanocages as a hybrid binder for CO2 capture

Applied Materials Today 51 (2026) 103295

Contents lists available at ScienceDirect

Applied Materials Today

journal homepage: www.elsevier.com/locate/apmt

3D printing of hierarchically porous MOF monoliths using silica nanocages as a hybrid binder for CO_2 capture

Thomas Gaillard [a,1], Arianna Bertero [b,1], Mathilde Ficheux [a], Philippe Trens [a], Julien Schmitt [a], Bartolomeo Coppola [b,*], Tangi Aubert [a,*]

[a] ICGM, Univ Montpellier, CNRS, ENSCM, Montpellier, France
[b] INSTM R.U PoliTO-LINCE Laboratory, Department of Applied Science and Technology, Politecnico di Torino, 10129 Turin, Italy

ARTICLE INFO

Keywords:
Additive manufacturing
Stereolithography
Nano-ink
Cu-BTC
CO_2 sorption

ABSTRACT

Metal-organic frameworks (MOFs), such as HKUST-1, are highly promising for carbon capture and storage due to their exceptional porosity and tunable properties. However, integrating MOFs into scalable, hierarchical structures, especially via 3D printing, has been challenging. Traditional 3D printing methods often rely on polymeric binders that block pore accessibility and require high-temperature processing, which degrades MOFs and limits their functionality. This work introduces a novel approach using digital light processing (DLP) 3D printing to fabricate MOF-containing monoliths with multiscale porosity. By replacing polymeric binders with methacrylate-functionalized silica nanocages, printable MOF/SiO_2 inks were obtained while preserving the microporosity and functionality of HKUST-1. Optimizing ink formulations enabled the printing of complex geometries, such as Gyroid structures, with high MOF content and high CO_2 affinity. The resulting MOF@SiO_2 composite materials have a hierarchical structure that combines the readily available micropores of the MOF with the mesopores of the silica scaffold and the macropores resulting from the geometrical design. This architecture ensures high accessibility to active sites, making the material ideal for flow-based application. Additionally, the method allows for post-printing functionalization, such as an additional in situ MOF growth, to further enhance porosity and sorption performance. This versatile approach overcomes the limitations for the printing of MOF-based materials, offering a transformative tool for designing advanced porous monolithic reactors.

1. Introduction

Human activities have been recognized as a major driver of disruption for several environmental markers through the emission of various pollutants. As a result, the development of effective technologies for environmental mitigation has become a critical priority. Material science plays an important role in this matter, enabling the development of catalytic materials for cleaner production processes [1], and sorbent materials for post-process remediation strategies [2]. In the last decades, scientific research on porous structures able to capture and/or separate pollutants has seen a significant rise, exploring materials such as activated carbons [3], mesoporous silica materials [4], and zeolites [5]. The performance of these materials strongly relies on a precise control of their porous architecture, which directly influence key parameters, including flow resistance and diffusivity to active sites [6]. Achieving this level of control requires a tailoring of the pores across several length scales, from micropores (< 2 nm) to macropores (up to several hundreds of μm). However, mastering such hierarchical structures remains challenging as most micro- and mesoporous materials are typically obtained as bulk powders. For practical applications, e.g. in continuous flow systems, these materials would strongly benefit from integration into monolithic structures featuring large (> 100 μm), interconnected macropores to limit potential pressure drops.

Among porous materials, metal organic frameworks (MOFs) have gained significant attention, as recently highlighted by a Nobel prize in chemistry [7]. These materials offer highly porous and tunable architectures that make them valuable for a wide range of applications, including in medicine [8], catalysis [9], separation technologies [10], and environmental applications [11,12]. For instance, HKUST−1, a copper-based MOF, exhibits very high specific surface areas and shows good affinity with the quadrupole moment of CO_2 thanks to its copper sites, making it suitable for carbon capture and storage technologies

* Corresponding authors.
E-mail addresses: bartolomeo.coppola@polito.it (B. Coppola), tangi.aubert@umontpellier.fr (T. Aubert).
[1] These authors contributed equally to this work.

https://doi.org/10.1016/j.apmt.2026.103295
Received 18 March 2026; Received in revised form 19 May 2026; Accepted 31 May 2026
Available online 5 June 2026

[13]. MOFs have attracted extensive research due to their exceptional potential, resulting in major advancements that position them as strong candidates for addressing key technological challenges. These breakthroughs are now driving the development of scalable production routes to enable their deployment in functional applications at industrial quantities [14]. However, MOF powders, typically made of sub-micrometric particles, pose significant limitations for practical implementation, causing in particular significant back-pressure drops or uneven fluid transport pathways in flow applications [14]. There is therefore a need to shape MOF-based materials into more practical and better-performing macroscopic structures for industrial applications. Various strategies have been reported for the integration of MOFs into hierarchical monoliths, including the synthesis of MOF gels featuring meso/macroporosities [12,15,16]. However, in this approach the produced monoliths often lack multiscale control over porosity, as both MOF and monolithic structure are synthesized simultaneously, and macroporosity is typically limited to a few micrometers with little structural control at the $>$ 100 μm to millimeter scale. An alternative approach involves growing MOFs on the surface of pre-existing meso and/or macroporous monolithic supports [17,18]. In such case, the macroporosity can be tailored independently from the MOF synthesis, but the volume of these supports often do not contribute to the overall sorption properties, as the MOF can only grow on its external surface. Therefore, the development of new approaches for the processing of MOFs with high control over multiscale porosity would significantly enhance pore accessibility and sorption performances. In that regard, the emergence of 3D printing for the engineering of advanced materials offers compelling opportunities.

3D printing has been thriving in the recent years, allowing the creation of highly complex architectures. Among these techniques, digital light processing (DLP) stands out as a versatile method, allowing the printing of structures with resolutions down to few tens of micrometers from a variety of materials, including ceramics, conductive materials or porous frameworks [19–21]. This method also allows for the parallel fabrication of multiple parts without increasing printing time. A major advantage of additive manufacturing is its virtually scale-independent production cost [22]. Additionally, its minimal waste generation makes the process environmentally friendly, giving it a sustainability edge over conventional manufacturing. Thus, additive manufacturing through DLP printing has moved beyond prototyping and is now a relevant approach for the production of advanced and highly engineered materials. Nevertheless, despite the potential synergy, reports on DLP printing of highly porous MOF materials remain scarce. 3D printing of MOF-based materials has mostly been achieved through direct ink writing techniques [23,24]. While this approach can produce structures with high readily accessible porosity, it suffers from limited resolution and restricted geometric freedom. Some highly detailed structures containing MOFs have been achieved through DLP approaches [25,26]. However, these structures typically consist of MOFs embedded in polymers, which significantly hinder pore accessibility. Currently, the integration of functional materials with DLP is typically achieved by formulating composite resins in which active fillers are dispersed within photosensitive organic binders. Upon UV/blue light irradiation, these binders polymerize into a dense matrix. For porous materials, this organic matrix must thereafter be removed to restore pore accessibility through a debinding or calcination step, which generally requires temperatures above 400 °C to be effective. However, MOFs, which also contain an organic component, cannot withstand such elevated temperatures and instead undergo complete degradation, resulting in the loss of their functional properties. The development of a new approach for DLP printing of MOFs that preserves pore accessibility would therefore represent a significant advancement. It would enable the creation of a large variety of advanced sorbents, leveraging the extensive library of MOFs available in the literature.

In alternative to conventional polymer-based strategies for DLP printing of functional materials, UV-activated nano-inks composed of cross-linkable nanoparticles were developed. In particular, colloidal silica nanocages functionalized with methacrylate ligands enable the direct 3D printing of hierarchically porous silica structures [27,28]. This approach circumvents the issue related to polymer-containing formulations in 3D printing by replacing them with photo-sensitive surface ligands, thus reducing the organic content to its bare minimum. As a result, the printed materials exhibit intrinsic mesoporosity without requiring any calcination step. This makes such nano-inks an ideal platform to create 3D printed porous matrices, using the silica nanocage as porous binder for otherwise non-printable porous materials such as MOFs.

Herein, it is demonstrated that such silica nanocages can replace polymeric binders in composite resins, thereby enabling the direct DLP printing of MOF-containing materials with readily accessible microporosity throughout the entire 3D structure. To this end, novel MOF/SiO_2 inks were developed by combining methacrylate-functionalized silica nanocages with pre-synthesized HKUST−1 crystals. The effect of MOF loading on printability was systematically investigated, and both ink formulation and printing parameters were optimized to maximize the active component content while ensuring reliable and accurate printing. Using these inks, monolithic MOF@SiO_2 structures with complex geometries were successfully fabricated. These composite structures showcase a highly hierarchical architecture, featuring macropores from the 3D printing process, mesopores from the silica framework, and micropores from the MOF. It is also demonstrated how the intrinsic porosity of the printed material can be used for the in situ growth of additional MOF within the monolith, highlighting the complementarity of this strategy with other existing approaches. Finally, the potential of these material for carbon capture and storage technologies is evidenced through CO_2 sorption measurements. By reducing the risk of back pressure drop, the shaping of these MOF-based materials into monolithic Gyroid structures make them particularly relevant for in flow application.

2. Results and discussion

2.1. Formulation of the functional MOF/SiO_2 inks

This work introduces a novel ink formulation designed to enable the direct 3D printing of MOF-containing monoliths. In this ink design, HKUST−1 crystals are incorporated alongside silica nanocages (Fig. 1a), where the nanocages act as a porous hybrid binder to immobilize the functional MOF within the printed structure. To formulate these inks, 13 nm silica nanocages (Fig. 1b) were first synthesized through a micelle templated sol-gel process [29], and functionalized with methacrylate ligands based on previously reported protocols [27,28]. These nanocages were dispersed in propylene carbonate, a non-toxic and non-volatile solvent well-suited for DLP 3D printing, yielding a clear and scatter-free solution (Fig. 1c). In parallel, HKUST−1 crystals were synthesized separately based on a previously reported ethanol-water mixture protocol, which avoids harmful organic solvents [30]. This synthesis method produces micrometric octahedral crystals, as observed via scanning electron microscope (SEM) (Fig. 1d). Their crystalline structure, consistent with HKUST−1, was confirmed by XRD analyses (Fig. S1 Supporting Information). After drying overnight at 120 °C to remove any adsorbed moisture, the MOF crystals were dispersed in the silica nanocage solution via magnetic stirring, resulting in homogeneous suspensions with a deep blue color, characteristic of HKUST−1 (Fig. 1e). The ink formulation was completed with phenylbis(2,4,6-trimethylbenzoyl)phosphine oxide (BAPO, 20 mM), which has proven to be an efficient photoinitiator for DLP printing with silica nanocage inks [27].

While the silica nanocages themselves show excellent colloidal stability in propylene carbonate, the micrometric MOF crystals on the other hand gradually sedimented over time, resulting in non-homogeneous suspensions after one hour without stirring (Fig. S2 Supporting

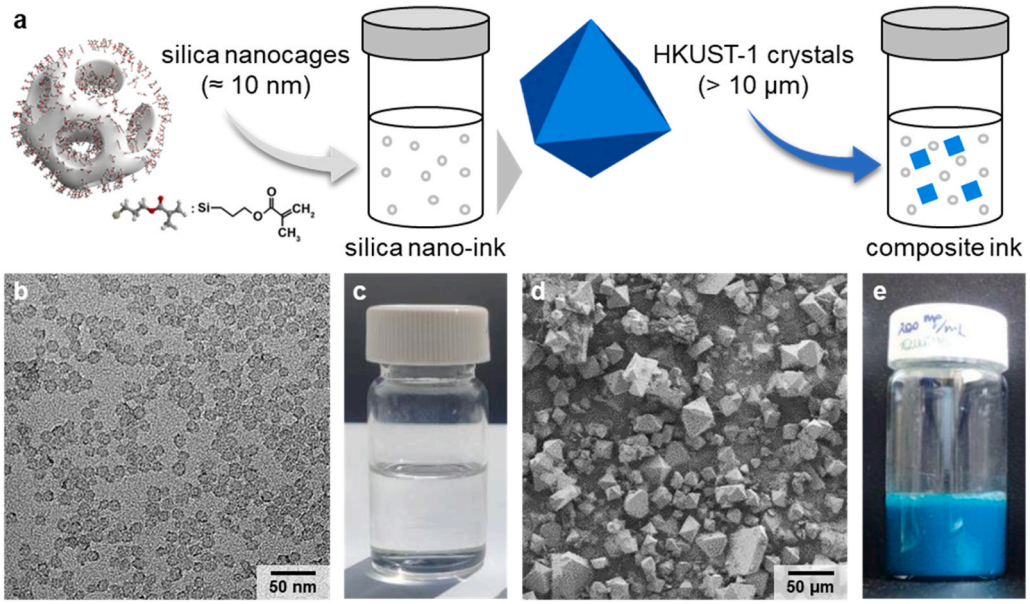

Fig. 1. (a) Illustration of the MOF/SiO_2 ink formulation. (b) TEM image of the methacrylate-functionalized silica nanocages and (c) picture of their suspension in propylene carbonate. (d) SEM image of HKUST−1 crystals. (e) Picture of a MOF/SiO_2 ink.

Information). This sedimentation effect can be problematic for standard vat-based DLP systems as the ink typically remains static for several hours during the printing process, making such formulations unsuitable for conventional DLP devices. To address this limitation, we used a DLP 3D printer equipped with a rolling foil (Admaflex 130, Admatec). Unlike standard DLP systems that rely on a static vat, this printer spreads the ink from an ink reservoir onto the printing bed using a moving foil (Fig. S3 Supporting Information). The mechanical movement, occurring

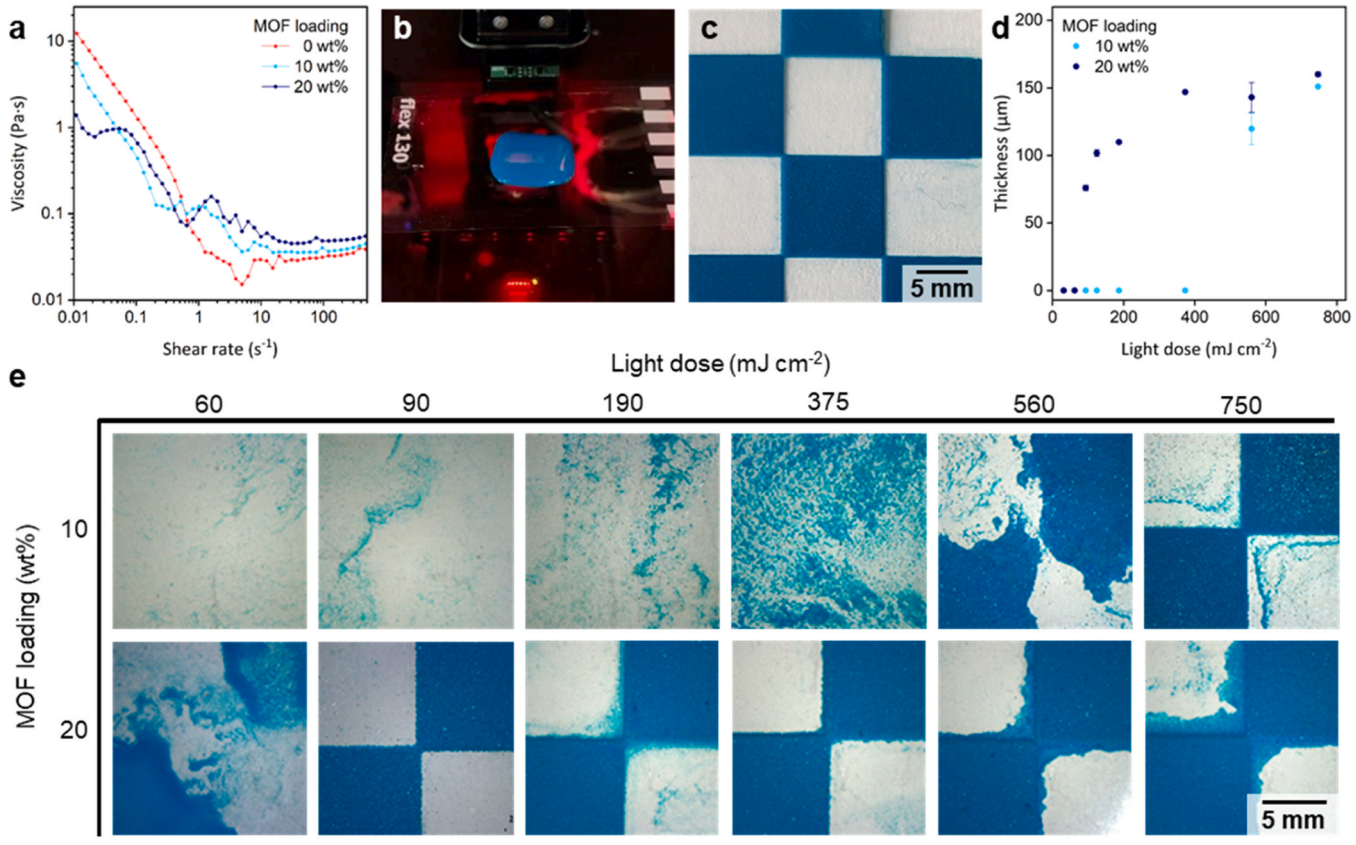

Fig. 2. (a) Viscosity of the ink as a function of MOF loading. (b) Picture of MOF/SiO_2 ink deposited onto the 3D printer rolling foil. (c) Picture of a typical checkerboard pattern printed to evaluate print accuracy and curing depth. (d) Layer thickness (mean value and standard deviation of three independent experiments) and (e) stereomicroscope images of printed layers as a function of the light dose and MOF loading. For all these experiments, the silica nanocage concentration was set to 100 mg•mL^{-1}.

between each printed layer helps mitigating sedimentation. Additionally, this setup can also be used with an external ink tank to ensure continuous homogenization during extended printing jobs.

2.2. Influence of the MOF loading on ink printability

Given the substantial size disparity between the silica nanocages (13 nm) and the MOF crystals (several tens of micrometers), it was essential to first assess how incorporating micrometric MOF crystals would affect printability. To this end, different MOF/SiO_2 inks were therefore prepared by adding 10 and 20 wt% of HKUST−1 to a silica nano-ink with an initial nanocage concentration of 100 mg•mL^{-1}. This MOF loading is defined as the weight fraction in the entire ink, i.e. including the solvent, so it differs from the loading in the final dried material, which is discussed later in the text. Attempts at increasing the MOF loading in the ink to 25 wt% yielded a very thick mixture, unsuitable for 3D printing. In contrast, the integration of 10 and 20 wt% of MOF only had a moderate impact on the ink rheology (Fig. 2a). The inks maintained their shear-thinning behavior, with viscosities at 150 s^{-1}, the shear rate value corresponding to the employed operative conditions of the Admaflex 130 printer, increasing from 32 mPa•s for a plain silica nanocage ink to 37 and 49 mPa•s for inks with MOF loadings of 10 and 20 wt%, respectively. While those viscosities are relatively low when compared to typical resin-based printing formulations, which often exceed 1000 mPa•s [31], they are particularly well suited for printing with silica nanocage inks. Indeed, for these nano-inks, it is crucial to maintain a low viscosity, as the printed parts remain fragile during the printing process, and excessive ink viscosity typically increases the risk of breakage during fabrication [27].

The effect of MOF loading on the curing depth and print accuracy was then investigated using these inks. To this end, a thick deposit of ink was manually spread onto the rolling foil (i.e. printing bed) of the 3D printer, as shown in Fig. 2b, and a checkerboard light pattern was projected. The sample was rinsed with ethanol to remove uncured ink, air dried overnight (Fig. 2c), and the thickness of the printed layer was measured using a digital micrometer to estimate the curing depth. Figs. 2d and 2e show that a minimum light dose is required for effective material curing. Specifically, ink with 20 wt% MOF loading yielded well printed layers at 90 mJ•cm^{-2}, whereas ink with 10 wt% MOF loading required a significantly higher dose of 560 mJ•cm^{-2}. Furthermore, the layers corresponding to 10 wt% MOF loading showcased poor resolution, as parts of the printed pattern were washed away during the ethanol rinsing (Fig. 2e). In contrast, the 20 wt% ink achieved complete layers with a well-defined pattern at 90 mJ•cm^{-2}, although overcuring effects emerged at much higher light doses. These findings suggest that MOF positively influences the printability of the functional inks by lowering the energy threshold required for effective printing. Previously, it was demonstrated that inks containing 100 mg•mL^{-1} of silica nanocages alone were insufficient for effective printing using a standard DLP printer [27], likely because at such a concentration the silica nanocages are too distant from each other for the formation of a solid 3D network. The addition of MOF in this case may help by compensating for the insufficient volume fraction of the nanocages. Increasing the MOF concentration hence decreases the interparticle distance, which promotes their cross-linking. Fig. 2d further shows that, beyond the printing threshold, the layer thickness initially increases with the light dose but eventually reaches a plateau at ca. 150 μm. Therefore, for subsequent experiments, the 20 wt% MOF-containing inks were selected, as this formulation both maximizes active component loading and facilitates printing with good resolution.

2.3. Influence of the nanocage concentration on ink printability

After evaluation of the impact of HKUST−1 loading, the influence of the silica nanocage concentration at high MOF loading was then examined. Curing tests were performed for MOF/SiO_2 inks containing 20 wt% of HKUST−1 and silica nanocage concentrations of 100, 150 and 200 mg•mL^{-1}. Fig. 3a shows that higher silica nanocage concentrations reduce the minimum light dose required for effective curing. In addition, while the layer thickness still increased with higher light doses, as already observed with varying MOF loadings, Fig. 3b reveals that layer thickness also increases with nanocage concentration. This enhanced curing depth can be attributed to the higher concentration of photosensitive methacrylate groups present in the ink. However, light doses above 375 mJ•cm^{-2} led to significant lateral overcuring (Fig. S4 Supporting Information), regardless of the ink concentration. Fig. 3c further indicates that at a nanocage concentration of 200 mg•mL^{-1}, the ink viscosity rises to 90 mPa·s (shear rate = 150 s^{-1}), which remains compatible with 3D printing using the Admaflex 130. In contrast, increasing the nanocage concentration to 250 mg•mL^{-1} resulted in a sharp viscosity increase (Fig. 3c), similar to what was observed for plain silica nanocage inks [27], rendering the formulation unsuitable for 3D printing. Consequently, 200 mg•mL^{-1} was identified as the upper limit of nanocage concentration that enables high curing depths while maintaining printability.

2.4. Large 3D printed MOF@SiO_2 composite structures

Guided by previous findings, 6 mm tall MOF@SiO_2 monoliths with a Gyroid structure were printed using an ink containing 200 mg•mL^{-1} silica nanocages and 20 wt% MOF (Fig. 4a). A light dose of 90 mJ•cm^{-2} per layer was employed, as this value provided an optimal balance between sufficient curing depth, high printing accuracy, and a low risk of lateral overcuring. After printing, the structures were thoroughly washed with ethanol and methanol before being dried using supercritical CO_2 at 35 °C, 80 bar. The material exhibited a blue coloration and a granular surface with faceted light reflections (Fig. 4b), consistent with the characteristic morphology of the HKUST−1 crystals. SEM observations of a fractured piece of the Gyroid structure confirmed the presence of well-preserved MOF crystals embedded in the matrix of silica nanocages (Fig. 4c). XRD analyses of the printed composite material further displayed sharp peaks consistent with HKUST−1 structure (Fig. S5 Supporting Information), confirming that the MOF crystallinity is not altered throughout the printing process. EDX analyses indicated a Cu:Si atomic ratio of 0.26, corresponding to a MOF content of approximately 40 wt% in the final printed material, that is after drying. This MOF content was estimated from the Cu:Si atomic ratio by accounting for the stoichiometries of SiO_2 (Mw = 60 g•mol^{-1}) and $C_{18}H_{12}Cu_3O_{15}$ (Mw = 659 g•mol^{-1}) for silica and HKUST−1, respectively. The calculation also takes into account that the methacrylate ligands typically constitute 36 wt% of a plain 3D printed silica nanocage monolith, as previously determined [27]. From an ink containing 200 mg•mL^{-1} silica nanocages and 20 wt% MOF, a maximal MOF loading of 60 wt% in the final material (after solvent removal) could have been expected, suggesting that some MOF might be washed out from the silica framework during cleaning with alcohols after printing. Nevertheless, no significant leaching of the MOF was observed after the first solvent exchanges, suggesting that the MOF fraction that remain in the printed part is firmly trapped in the material.

The textural properties of the printed parts were characterized by nitrogen sorption at 77 K. The MOF@SiO_2 composite material exhibited a combination of type I and IV isotherms (Fig. 4d), characteristic of the microporosity of HKUST−1 and of the mesoporosity of the silica scaffold, respectively [32], underlining the highly hierarchical material structure. Capillary condensation occurs at $P/P_0 = 0.98$, followed by a corresponding desorption at $P/P_0 = 0.95$, forming a hysteresis loop similar to that of a plain silica monolith. A BJH analysis of the isotherms suggests an increase in the pore size distribution, from 50 nm for the plain silica monolith to ca. 100 nm for the MOF@SiO_2 composite monolith (Fig. S6 Supporting Information). This relatively large mesoporosity arises from the dominant interparticle porosity formed during printing [27], which is likely further enlarged by the incorporation of

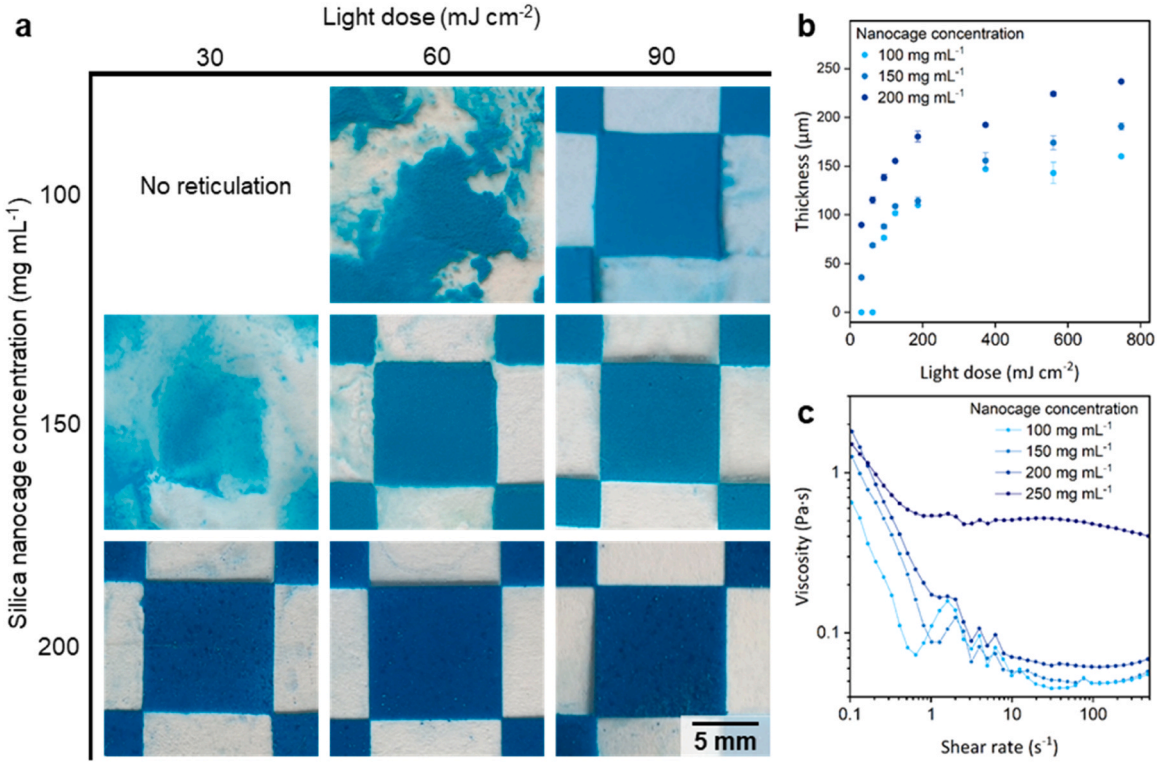

Fig. 3. (a) Pictures of checkerboard patterns printed at different light doses and different silica nanocage concentrations. (b) Thickness of printed layers as a function of light dose (mean value and standard deviation of three independent experiments). (**c**) Viscosity as a function of shear rate of inks with different silica nanocage concentrations.

the micrometric MOF crystals within the silica matrix. The MOF@SiO_2 monolith also shows a steady increase in gas uptake at very low relative pressure ($P/P_0 < 0.01$), a signature feature of type I isotherms that reflect the high microporosity of the MOF. Because the BJH method only applies to mesopores and small macropores, DFT or NLDFT methods would be needed to estimate the MOF micropore size distribution [32]. While dedicated models are not readily available for MOF@SiO_2 composite materials, a generic DFT model was applied to the N_2 adsorption isotherms of the MOF alone, and the MOF@SiO_2 composite materials, indicating in all cases the presence of pores in the expected range for HKUST−1 around 1 nm (Fig. S7 Supporting Information). However, due to the limited validity of the model these analyses could not be discussed in further details. In addition, the specific surface area concomitantly increases from ca. 500 $m^2 \bullet g^{-1}$ for plain silica monoliths to 1200 $m^2 \bullet g^{-1}$ for MOF@SiO_2 composite monoliths. Interestingly, the as-synthesized HKUST−1 powder exhibits a specific surface area of only 850 $m^2 \bullet g^{-1}$ (Fig. S8 in the Supporting Information). During fabrication, the MOF powder is dispersed in propylene carbonate, and the printed materials are washed with ethanol, soaked in methanol for at least three days, and finally dried with supercritical CO_2. These steps can enhance the specific surface area of MOF materials. In particular, supercritical CO_2 has been reported as highly effective for MOF activation, leading to significant increases in specific surface area values [34]. It outperforms conventional activation (heating under vacuum) or solvent exchange activation methods, as supercritical CO_2 efficiently removes guest molecules and impurities from MOFs after synthesis. To illustrate this, some of the as-synthesized HKUST−1 powder was subjected to the same treatment as the printed material, resulting in an increase in specific surface area from 850 to 1800 $m^2 \bullet g^{-1}$ (Fig. S8 Supporting Information). While this value does not fully account for the 1200 $m^2 \bullet g^{-1}$ specific surface area of the MOF@SiO_2 material considering the MOF:SiO_2 = 0.4:0.6 composition, we hypothesize that the supercritical CO_2 activation mechanism may be even more efficient when the MOF is homogeneously dispersed and supported on the porous silica scaffold. These findings confirm that the MOF microporosity remains greatly accessible even when embedded within the silica nanocage matrix. This highlights the critical role of the silica nanocages as a porous binder for the MOF crystals, without compromising their pore and surface accessibility.

The CO_2 sorption performances of the printed MOF@SiO_2 parts were evaluated at 298 K (Fig. 4e). The composite material exhibits a high affinity for CO_2, reaching a total sorption capacity of 0.98 mmol$\bullet g^{-1}$ at 1 bar as compared to 0.33 mmol$\bullet g^{-1}$ for the plain silica structure. This property is directly enabled by the efficient integration of HKUST−1, making the resulting composite 3D structures highly valuable for carbon capture technologies.

2.5. *Additional post-printing in situ MOF growth*

In previous studies, we demonstrated that MOFs could also be directly grown on 3D printed substrates through a post-printing process [27,33]. These approaches often required repeated growth steps and were limited to MOF loadings of only a few wt% for non-porous substrates and 30 wt% for porous substrates. In contrast, the approach presented here enables substantially higher MOF loadings, with up to 40 wt% of MOF in the dried material, achieved directly during the printing process. Notwithstanding this advancement, the intrinsic porosity of the silica nanocage matrix provides additional free volume that can accommodate further MOF formation. On this basis, we investigated a post-printing in situ MOF growth strategy to further increase the sorption capacity of the 3D printed MOF@SiO_2 monoliths. This additional growth was performed directly after printing (i.e. before drying) and was adapted from a previously reported MOF growth on 3D printed inorganic scaffolds (see Experimental Section for details) [33]. The process leverages the available multiscale porosity from the printed Gyroid structure, allowing the MOF precursors to diffuse throughout the material. After a subsequent thermal treatment at 120 °C for 6 h, the

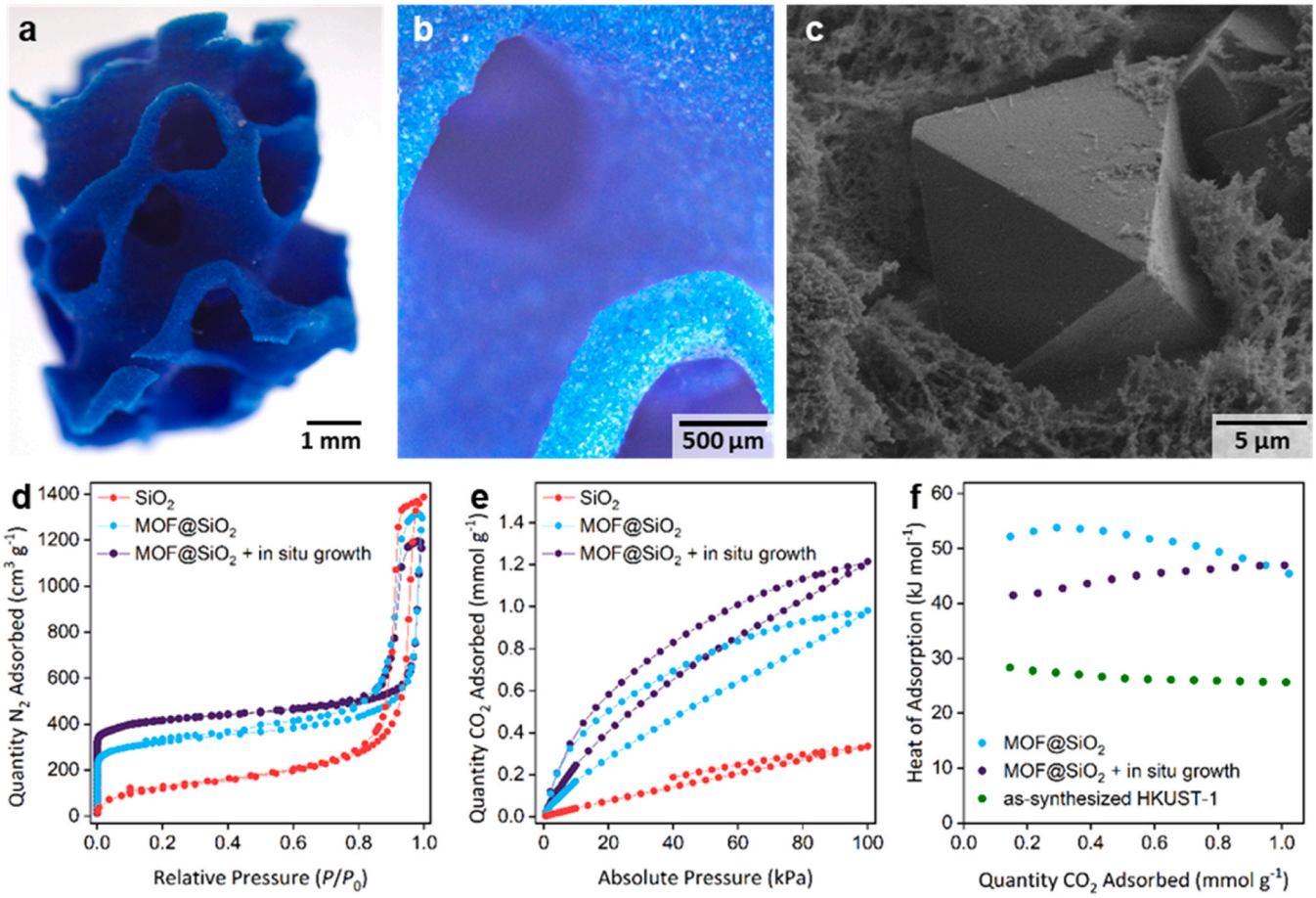

Fig. 4. (a,b) Stereomicroscope images at different magnifications of a 3D printed MOF@SiO_2 composite Gyroid. (c) SEM image of a fractured piece, showing the inside of the composite Gyroid. (d) Nitrogen sorption (77 K), and (e) CO_2 sorption (298 K) isotherms of 3D printed plain silica and composite materials before and after an additional in situ MOF growth. (f) Isosteric heat of CO_2 adsorption of the composite materials compared to the as-synthesized MOF powder.

monoliths were further washed and dried using supercritical CO_2, following the same protocol previously described. EDX analyses indicated a Cu:Si molar ratio of 0.42, corresponding to an increase in the MOF loading from the initial 40 wt% in the dried, printed material to ca. 50 wt%. The impact on textural and functional properties was also evaluated through N_2 and CO_2 sorption measurements. The N_2 sorption isotherms exhibit a very similar shape to that of the initial MOF@SiO_2 material (Fig. 4d), indicating that mesoporosity is preserved. Notably, the gas uptake at low relative pressure ($P/P_0 < 0.01$) is increased, indicating an enhancement of the microporosity. This observation aligns with the increase in MOF loading within the material. Consequently, the specific surface area also increased from 1200 $m^2 \bullet g^{-1}$ to 1600 $m^2 \bullet g^{-1}$ after additional MOF growth. The specific total pore volume decreased from 2.0 $cm^3 \bullet g^{-1}$ to 1.8 $cm^3 \bullet g^{-1}$, but this does not reflect a reduction in the absolute total pore volume of the monolithic structure, as this variation accounts for the weight increase from the additional MOF growth. In addition, a BJH analysis of the pore size distribution confirmed that mesoporosity remained mostly unchanged (Fig. S6 Supporting Information), which indicates that it was not completely filled with MOF and remains available to facilitate fluid transport through the material. The CO_2 sorption capacity at 298 K and 1 bar further increased to 1.21 mmol$\bullet g^{-1}$ (Fig. 4e). Given that the material contains 50 wt% MOF, this CO_2 sorption capacity corresponds to approximately 2.4 mmol per gram of MOF. This value falls within the typical range for HKUST−1, which has been reported with sorption capacities of 1–4 mmol/g under comparable temperature and pressure conditions [35]. Prior to the additional in situ MOF growth, the material also exhibited a CO_2 sorption capacity of about 2.4 mmol per gram of MOF. Thus, while the in situ growth step does not change the sorption capacity of embedded MOF, the increased MOF loading enhances the material overall performance. We note however, that the as-synthesized MOF exhibits a sorption capacity of 3.4 mmol$\bullet g^{-1}$ (Fig. S9 Supporting Information). While this observation is not fully understood yet, it could indicate that the beneficial effect of supercritical CO_2 activation on the MOF specific surface area could actually have a slightly detrimental effect on its CO_2 sorption capacity. On the other hand, we also measured the CO_2 adsorption kinetics at 298 K under atmospheric pressure using a dynamic vapor sorption system (Fig. S10 Supporting Information). In this case, all the samples, including as-synthesized MOF and the MOF@SiO_2 materials, exhibited rapid and virtually identical CO_2 adsorption rates, reaching 90% of equilibrium uptake within 5 min under CO_2 flow. The high similarity in adsorption rate confirms that the CO_2 adsorption sites remain fully accessible in the MOF@SiO_2 materials. These adsorption kinetics data were best fitted with a pseudo-first-order model rather than with a pseudo-second-order model (Fig. S10 Supporting Information), suggesting a direct proportionality between adsorption rate and the number of possible adsorption sites [36]. Thus, the new MOF processing approach reported here readily produces materials with high sorption capacity and remains compatible with other post-printing functionalization and in situ growth approaches developed separately, hence offering high complementarity for the fabrication of advanced porous and functional monolithic reactors.

2.6. *Isosteric heat of CO_2 adsorption*

CO_2 sorption analyses were also conducted at 283 and 273 K (in

addition to the 298 K measurements in Fig. 4e) for the MOF@SiO_2 materials and the as-synthesized MOF powder (Fig. S9 Supporting Information). From these analyses, the isosteric heat of adsorption was calculated using the Clausius-Clapeyron equation (Fig. 4f) [37]. For all systems, the isosteric heat remained nearly constant with increasing CO_2 uptake, indicating homogeneous MOF structures with equivalent adsorption sites. For the as-synthesized MOF powder, the zero coverage isosteric heat was estimated to ca. 30 kJ•mol^{-1}, consistent with typical values reported for HKUST−1 [38] and highlighting its strong CO_2 affinity. Incorporating the MOF in the silica matrix significantly increased this value to ca. 50 kJ•mol^{-1} (Fig. 4f), demonstrating an enhanced CO_2 affinity in the composite material. This significant increase in isosteric heat may reflect another consequence of the MOF activation with supercritical CO_2. While a similar high zero coverage value has been reported for another MOF@SiO_2 material [39], in this system the heat value was sharply decreasing with increasing amounts of adsorbed CO_2. Here, the 3D printed MOF@SiO_2 materials maintained a stable isosteric heat, suggesting a uniform distribution of the MOF crystals within the porous silica matrix and consistent accessibility of the adsorption sites throughout the material. The additional in situ HKUST−1 growth step performed on the MOF@SiO_2 structure, on the other hand, induced a reduction of the isosteric heat of adsorption, with a zero-coverage value estimated to ca. 40 kJ•mol^{-1}. It is noteworthy, however, that at high CO_2 uptake both composite MOF@SiO_2 materials, with and without in situ MOF growth, exhibit similar isosteric heats of adsorption, indicating comparable adsorption behavior under near-saturation conditions.

3. Conclusions

In this work, a novel strategy for the processing of MOFs via digital light processing 3D printing is introduced. Using porous silica nanocages instead of polymers as structural binder, a printable formulation allowing the direct printing of MOF-based materials with readily accessible microporosity was developed. Printing parameters optimization allowed the fabrication of complex, self-supporting architectures such as Gyroid structures. This triply periodic minimal surface geometry is particularly well suited for flow-based applications that can exploit the intrinsic properties of MOFs. Gas sorption analyses confirmed the multiscale porosity and high specific surface area of the printed structures. Notably, the composite MOF@SiO_2 materials demonstrated high CO_2 storage capacity, which could be further enhanced through a secondary MOF growth step. Since the HKUST−1 synthesis employed in this work follows a simple and widely adopted protocol, this strategy can be easily adapted to other MOF systems. Preliminary experiments replacing HKUST−1 with MIL−101(Cr) in the MOF/SiO_2 ink formulation confirmed its printability, with a similar relationship between light dose and curing depth (Fig. S11 Supporting Information). This versatility therefore opens opportunities to design a broad range of MOF@SiO_2 composite materials tailored to meet specific needs in catalytic, adsorption or environmental applications. The successful use of micrometric MOF powders suggests that this strategy is not constrained by strict granulometric requirements. It can be extended to various functional materials, broadening the potential of 3D printing across diverse fields where tailored material architectures are essential, including in catalysis, energy storage, separation technologies, and beyond. This work paves the way for the advancement of the design and application of next-generation porous materials and monolithic reactors.

4. Experimental section

4.1. Materials

Tetramethyl orthosilicate (TMOS, 98%), 1,3,5-trimethylbenzene (TMB, 98%), ammonia solution (28–30% in water), hexadecyltrimethylammonium bromide (CTAB, >99%), 3-(trimethoxysilyl)propyl methacrylate (TPM, 98%), propylene carbonate (99%), phenylbis(2,4,6-trimethylbenzoyl)phosphine oxide (BAPO, 97%), copper(II)nitrate hemi (pentahydrate) (98%), and benzene−1,3,5-tricarboxylic acid (BTC, 95%) were purchased from Sigma–Aldrich. Ethanol (96%) was purchased from Carlo Erba, and methanol (98.5%) from VWR. Deionized water with a resistivity of 18 MΩ was used throughout this work.

4.2. Synthesis of silica nanocages

The synthesis of the silica nanocages and their functionalization with methacrylate ligands was performed following a previously reported protocol that enabled the scaling of this synthesis to the liter scale [27]. Briefly, 12.5 g of CTAB was dissolved in 1 L of deionized water under gentle heating using a heat gun until a clear solution was obtained. 240 μL of ammonia solution and 10 mL of TMB were then added under magnetic stirring. After 4 h at room temperature, 10 mL of TMOS was added dropwise, and the reaction mixture was stirred overnight. 10 mL of TPM was subsequently added, and the synthesis was kept under stirring for an additional day. The resulting nanocages were precipitated by adding 2 L of ethanol and collected by centrifugation (5 min, 2000 g). The precipitate was redispersed in 200 mL of ethanol, yielding a stable and transparent suspension. This suspension was further washed twice with ethanol using centrifugal concentrators (Vivaspin 20, 100 kDa MWCO) and concentrated to a final volume of about 50 mL. The final concentration of silica nanocages was determined by drying and weighing a known volume of the resulting solution. This procedure yields about 6 g of methacrylate functionalized silica nanocages, and was typically performed twice to produce sufficient material for the formulation of a 75 g ink batch with 200 mg•mL^{-1} nanocages.

4.3. Synthesis of HKUST−1 crystals

HKUST−1 crystals were synthesized following a previously reported protocol [30]. For a typical synthesis, 0.7 g of trimesic acid (BTC) was dissolved in 20 mL of ethanol under gentle magnetic stirring. Concurrently, 1.44 g of copper(II) nitrate hemi(pentahydrate) was dissolved in 20 mL of water. After 10 min, the copper solution was added dropwise to the BTC solution. The mixture was kept under stirring for an additional 30 min. The reaction medium was then transferred to an 80 mL Teflon-line autoclave, which was sealed and placed in an oven at 120 °C for 6 h. The synthesis yielded typical blue HKUST−1 crystals, which were collected from the bottom of the autoclave. The MOF crystals were recovered by filtration on a Buchner, washed three times with water and ethanol and dried in an oven at 120 °C overnight before being stored in an airtight container. Prior to their use in printing formulations, HKUST−1 crystals were further dried overnight in an oven at 120 °C to eliminate residual moisture and prevent water incorporation in the inks. This procedure yields about 1 g of HKUST−1, and was typically performed 15 times using several autoclaves in parallel to produce sufficient material for the formulation of a 75 g ink batch with 20 wt% MOF.

4.4. Formulation of MOF/SiO_2 inks

For ink preparation, a calculated volume of silica nanocages suspension was mixed with propylene carbonate, and ethanol was removed using a rotary evaporator. The resulting mixture was transferred to graduated glassware, and its volume was adjusted with propylene carbonate to achieve the target concentration. BAPO was then added to reach a concentration of 20 mM. Finally, a weighted amount of dried HKUST−1 crystals was introduced to the solution to obtain the desired MOF wt% in the final formulation. The inks were kept under magnetic stirring overnight before use. To study the influence of MOF concentration, MOF were added to silica nanocage suspensions at 100 mg•mL^{-1} until reaching MOF loadings of 10, 20 and 25 wt%. To study the influence of silica nanocage concentration, different suspensions with 100, 150 and 200 mg•mL^{-1} were tested, and MOF were added to reach 20 wt% of the final ink.

4.5. DLP 3D printing

3D printing was carried out using an Admaflex 130 DLP printer (Admatec), equipped with a 405 nm LED and featuring a pixel size of approx. 50 μm. The optical power density of the 3D printer was set to 30 $mW \bullet cm^{-2}$ and the light dose was controlled by changing the exposure time, from 1 to 25 s. For the printing of large Gyroid structures, the layer thickness was set to 30 μm and the lift and down speeds of the printing platform were both set to 120 $mm \bullet min^{-1}$. After printing, the parts were rinsed with ethanol and stored in ethanol until drying or an eventual secondary growth step was performed.

4.6. Secondary in situ growth of MOF in printed monoliths

3D printed MOF@SiO_2 parts were immerged in a solution of 70 mg of BTC dissolved in 20 mL of ethanol. After 10 min, a solution of 144 mg of copper(II) nitrate hemi(pentahydrate) dissolved in 20 mL of water was added dropwise, and the mixture was kept under gentle stirring for an additional 30 min. The reaction medium as well as the printed parts were then carefully transferred to an 80 mL Teflon-line autoclave, which was sealed and placed in an oven at 120 °C for 6 h. The printed structures were rinsed with ethanol and kept in the alcohol until drying. The synthesis also produced a small quantity of blue HKUST−1 crystals at the bottom of the autoclave, which were not collected.

4.7. Drying of 3D printed structures

Before drying, the printed structures were transferred to methanol, which was replaced at least three times over three days. Finally, drying was performed using a Leica EM CPD300 critical point dryer under supercritical CO_2 conditions.

4.8. Characterization techniques

Rheological measurements were carried out using a Kinexus Pro + (Netzsch) equipped with 20 mm wide stainless steel parallel plates with a 1 mm gap. The temperature was maintained at 25 °C through the analysis using a Peltier module. Stereomicroscopy images were acquired using a Leica EZ4 W microscope. Transmission electron microscopy (TEM) images were acquired using a Jeol JEM−1400 Plus microscope operating at 100 kV (MEA platform, Université de Montpellier). Scanning electron microscopy (SEM) images were acquired using a Hitachi S4800 microscope operating at 5 kV. EDX analyses were performed using a Zeiss Sigma 300 microscope equipped with a X-Max^N 50 SDD detector (Oxford Instruments). Powder X-ray diffraction (XRD) analyses were performed using a D8 Advance (Bruker) diffractometer equipped with a Lynx eyes detector operating at 40 kV and 40 mA, and using a Cu radiation source. Gas sorption analyses were conducted at 77 K for N_2 and at 273, 283 or 298 K for CO_2 gases. For plain silica monoliths, prior to analyses the samples were degassed for 6 h at 50 °C and analyzed with a Tristar II Plus (Micromeritics). The as-synthesized HKUST−1 powder and composite monoliths containing MOF were analyzed by nitrogen sorption using a 3Flex (Micromeritics), which allowed characterizing the microporosity, and using a Tristar II Plus for CO_2 sorption. In this case, the samples were degassed at 150 °C during 24 h at a pressure below 1 Pa using a Smart Vac Prep bench (Micromeritics). For plain silica monoliths, the specific surface area (S_{BET}) was calculated using the Brunauer Emmett and Teller (BET) theory with five points. For HKUST−1 powder and MOF@SiO_2 composite monoliths, the specific surface area was estimated following the Rouquerol criteria, in accordance with the IUPAC recommendation for combination of type I and IV isotherms [32]. For pore width estimation in the mesoporous range, the Barrett-Joyner-Halenda-Broekhoff and de Boer (BJH-BdB) model was used on the adsorption branch of the isotherms, which is more suited for such materials with highly constricted pores [40]. For pore width estimation in the microporous range, a DFT model (MicroActive, N2 - DFT Model) was applied on the N_2 adsorption branch up to $P/P_0 = 0.01$. The isosteric heat of adsorption was determined from CO_2 sorption isotherms measured at 273, 283 and 298 K. Experimental data were fitted using the MicroActive software (Micromeritics) to obtain equilibrium pressures for the three isotherms at 15 identical relative pressures, and the isosteric heat of adsorption was calculated using the Clausius-Clapeyron equation by plotting ln(P) as a function of 1/T. The CO_2 adsorption kinetic data were obtained using Dynamic Vapour Sorption (DVS, SMS Resolution) instrument with a microbalance sensitivity of 0.1 μg. After activation at 150 °C for 12 h under nitrogen flow, the sample was cooled down to 25 °C and exposed to a constant CO_2 flow at (at a rate of 200 $mL \bullet min^{-1}$).

CRediT authorship contribution statement

Tangi Aubert: Writing – review & editing, Supervision, Methodology, Funding acquisition, Formal analysis, Conceptualization. **Bartolomeo Coppola:** Writing – review & editing, Supervision, Methodology, Funding acquisition, Formal analysis, Conceptualization. **Julien Schmitt:** Writing – review & editing, Supervision, Methodology, Funding acquisition, Formal analysis, Conceptualization. **Philippe Trens:** Formal analysis, Investigation, Methodology, Writing – review & editing. **Mathilde Ficheux:** Investigation, Methodology, Writing – review & editing. **Arianna Bertero:** Writing – review & editing, Methodology, Investigation, Formal analysis. **Thomas Gaillard:** Writing – original draft, Methodology, Investigation, Formal analysis.

Declaration of Generative AI in the manuscript preparation process

During the preparation of this work the authors used the generative AI tool *Emmy* in order to improve language and readability. After using this tool, the authors reviewed and edited the content as needed and take full responsibility for the content of the published article.

Declaration of Competing Interest

The authors declare that they have no known competing financial interests or personal relationships that could have appeared to influence the work reported in this paper.

Acknowledgement

The authors acknowledge Nicolas Brun for providing technical support with CO_2 sorption analyses, and Bertrand Rebière for SEM and EDX analyses. The authors acknowledge Franck Godiard from the MEA platform, Université de Montpellier, for assistance with TEM analyses. This work received funding from the Agence Nationale de la Recherche under grant number: ANR−21-CE08–0012−01. Part of the research carried out for this work was made possible thanks to the financial support of CNRS International Emerging Actions within the framework of the AMOUR Project.

Appendix. Supplementary materials

Additional experimental data including XRD analyses, nitrogen and CO_2 sorption and printability tests; Illustration of ink sedimentation and printing process.

Appendix A. Supporting information

Supplementary data associated with this article can be found in the online version at doi:10.1016/j.apmt.2026.103295.

Data Availability

Data will be made available on request.

References

[1] J. Liang, Z. Liang, R. Zou, Y. Zhao, Heterogeneous catalysis in zeolites, mesoporous silica, and metal–organic frameworks, Adv. Mater. 29 (30) (2017) 1701139, https://doi.org/10.1002/adma.201701139.

[2] P. Samanta, A.V. Desai, S. Let, S.K. Ghosh, Advanced porous materials for sensing, capture and detoxification of organic pollutants toward water remediation, ACS Sustain. Chem. Eng. 7 (8) (2019) 7456–7478, https://doi.org/10.1021/acssuschemeng.9b00155.

[3] R. Zhu, J. Guo, H. Pang, D. Zhao, Q. Liu, P. Liang, Adsorption separation of gaseous pollutants over porous carbon materials: a review, J. Energy Inst. 120 (2025) 102129, https://doi.org/10.1016/j.joei.2025.102129.

[4] P.N.E. Diagboya, E.D. Dikio, Silica-based mesoporous materials; emerging designer adsorbents for aqueous pollutants removal and water treatment, Microporous Mesoporous Mater. 266 (2018) 252–267, https://doi.org/10.1016/j.micromeso.2018.03.008.

[5] Z. Tao, Y. Tian, W. Wu, Z. Liu, W. Fu, C.-W. Kung, J. Shang, Development of zeolite adsorbents for CO_2 separation in achieving carbon neutrality, npj Mater. Sustain. 2 (1) (2024) 20, https://doi.org/10.1038/s44296-024-00023-x.

[6] A. Galarneau, A. Sachse, B. Said, C.-H. Pelisson, P. Boscaro, N. Brun, L. Courtheoux, N. Olivi-Tran, B. Coasne, F. Fajula, Hierarchical porous silica monoliths: a novel class of microreactors for process intensification in catalysis and adsorption, Comptes Rendus. Chim. 19 (1–2) (2016) 231–247, https://doi.org/10.1016/j.crci.2015.05.017.

[7] J.E. Millstone, J.M. Buriak, X. Chen, L.M. Liz-Marzán, R.E. Schaak, A new landmark for reticular chemistry: celebrating the nobel prize for metal–organic frameworks, ACS Nano 19 (44) (2025) 38187–38188, https://doi.org/10.1021/acsnano.5c18333.

[8] X. Ge, R. Wong, A. Anisa, S. Ma, Recent development of metal-organic framework nanocomposites for biomedical applications, Biomaterials 281 (2022) 121322, https://doi.org/10.1016/j.biomaterials.2021.121322.

[9] G.-J. Lee, Y.-W. Chien, S. Anandan, C. Lv, J. Dong, J.J. Wu, Fabrication of metal-doped bioi/mof composite photocatalysts with enhanced photocatalytic performance, Int. J. Hydrog. Energy 46 (8) (2021) 5949–5962, https://doi.org/10.1016/j.ijhydene.2020.03.254.

[10] Y.-L. Zhao, Q. Chen, X. Zhang, J.-R. Li, Enabling C2H2/CO_2 separation under humid conditions with a methylated copper MOF, Adv. Sci. 11 (17) (2024) 2310025, https://doi.org/10.1002/advs.202310025.

[11] S. Mahajan, M. Lahtinen, Recent progress in metal-organic frameworks (MOFs) for CO_2 capture at different pressures, J. Environ. Chem. Eng. 10 (6) (2022) 108930, https://doi.org/10.1016/j.jece.2022.108930.

[12] C. Chen, L. Shen, B. Wang, X. Lu, S. Raza, J. Xu, B. Li, H. Lin, B. Chen, Environmental applications of metal–organic framework-based three-dimensional macrostructures: a review, Chem. Soc. Rev. 54 (5) (2025) 2208–2245, https://doi.org/10.1039/D4CS00435C.

[13] C. Prestipino, L. Regli, J.G. Vitillo, F. Bonino, A. Damin, C. Lamberti, A. Zecchina, P.L. Solari, K.O. Kongshaug, S. Bordiga, Local structure of framework Cu(II) in HKUST-1 metallorganic framework: spectroscopic characterization upon activation and interaction with adsorbates, Chem. Mater. 18 (5) (2006) 1337–1346, https://doi.org/10.1021/cm052191g.

[14] D. Chakraborty, A. Yurdusen, G. Mouchaham, F. Nouar, C. Serre, Large-scale production of metal–organic frameworks, Adv. Funct. Mater. 34 (43) (2024) 2309089, https://doi.org/10.1002/adfm.202309089.

[15] A. Ahmed, T. Hasell, R. Clowes, P. Myers, A.I. Cooper, H. Zhang, Aligned macroporous monoliths with intrinsic microporosity via a frozen-solvent-templating approach, Chem. Commun. 51 (9) (2015) 1717–1720, https://doi.org/10.1039/C4CC08919G.

[16] N. Moitra, S. Fukumoto, J. Reboul, K. Sumida, Y. Zhu, K. Nakanishi, S. Furukawa, S. Kitagawa, K. Kanamori, Mechanically stable, hierarchically porous Cu3(Btc)2 (HKUST-1) monoliths via direct conversion of copper(II) hydroxide-based monoliths, Chem. Commun. 51 (17) (2015) 3511–3514, https://doi.org/10.1039/C4CC09694K.

[17] H. Li, Y. Liu, F. He, H. Yang, Z. Li, Q. Zhou, K. Tang, Situ grown Cu-based metal-organic framework on copper foam as high-performance electrocatalysts for oxygen evolution reaction, Int. J. Hydrog. Energy 45 (41) (2020) 21540–21546, https://doi.org/10.1016/j.ijhydene.2020.05.234.

[18] A. Sachse, R. Ameloot, B. Coq, F. Fajula, B. Coasne, D.D. Vos, A. Galarneau, Situ synthesis of Cu–BTC (HKUST-1) in macro-/mesoporous silica monoliths for continuous flow catalysis, Chem. Commun. 48 (39) (2012) 4749–4751, https://doi.org/10.1039/C2CC17190B.

[19] B. Coppola, E. Fiume, V. Terranova, L. Montanaro, P. Palmero, Digital light processing of ceria-stabilized zirconia: role of powder pre-treatment on printability and physico-mechanical properties, J. Eur. Ceram. Soc. 45 (13) (2025) 117512, https://doi.org/10.1016/j.jeurceramsoc.2025.117512.

[20] S.-C. Tsai, L.-H. Chen, C.-P. Chu, W.-C. Chao, Y.-C. Liao, Photo curable resin for 3D printed conductive structures, Addit. Manuf. 51 (2022) 102590, https://doi.org/10.1016/j.addma.2021.102590.

[21] H. Zhang, P. Wang, H. Zhang, H. Yang, H. Wang, L. Zhang, Structured zeolite monoliths with ultrathin framework for fast CO_2 adsorption enabled by 3D printing, Ind. Eng. Chem. Res. 59 (17) (2020) 8223–8229, https://doi.org/10.1021/acs.iecr.9b07060.

[22] R. Chaudhary, P. Fabbri, E. Leoni, F. Mazzanti, R. Akbari, C. Antonini, Additive manufacturing by digital light processing: a review, Prog. Addit. Manuf. 8 (2) (2023) 331–351, https://doi.org/10.1007/s40964-022-00336-0.

[23] G.J.H. Lim, Y. Wu, B.B. Shah, J.J. Koh, C.K. Liu, D. Zhao, A.K. Cheetham, J. Wang, J. Ding, 3D-printing of pure metal–organic framework monoliths, ACS Mater. Lett. 1 (1) (2019) 147–153, https://doi.org/10.1021/acsmaterialslett.9b00069.

[24] W.Y. Lieu, D. Fang, K.J. Tay, X.L. Li, W.C. Chu, Y.S. Ang, D.-S. Li, L.-K. Ang, Y. Wang, H.Y. Yang, Progress on 3D-printed metal-organic frameworks with hierarchical structures, Adv. Mater. Technol. 7 (11) (2022) 2200023, https://doi.org/10.1002/admt.202200023.

[25] A. Pustovarenko, B. Seoane, E. Abou-Hamad, H.E. King, B.M. Weckhuysen, F. Kapteijn, J. Gascon, Rapid fabrication of MOF-based mixed matrix membranes through digital light processing, Mater. Adv. 2 (8) (2021) 2739–2749, https://doi.org/10.1039/D1MA00023C.

[26] O. Halevi, J.M.R. Tan, P.S. Lee, S. Magdassi, Hydrolytically stable MOF in 3D-printed structures, Adv. Sustain. Syst. 2 (2) (2018) 1700150, https://doi.org/10.1002/adsu.201700150.

[27] T. Gaillard, A. Bertero, C. Joly-Duhamel, C. Biolley, B. Coppola, N. Brun, A. Galarneau, T. Aubert, 3D printing of functional mesoporous silica monoliths with embedded metal and MOF components, Adv. Funct. Mater. 35 (48) (2025) 2509897, https://doi.org/10.1002/adfm.202509897.

[28] T. Aubert, J.-Y. Huang, K. Ma, T. Hanrath, U. Wiesner, Porous cage-derived nanomaterial inks for direct and internal three-dimensional printing, Nat. Commun. 11 (1) (2020) 4695, https://doi.org/10.1038/s41467-020-18495-5.

[29] K. Ma, Y. Gong, T. Aubert, M.Z. Turker, T. Kao, P.C. Doerschuk, U. Wiesner, Self-assembly of highly symmetrical, ultrasmall inorganic cages directed by surfactant micelles, Nature 558 (7711) (2018) 577–580, https://doi.org/10.1038/s41586-018-0221-0.

[30] K. Schlichte, T. Kratzke, S. Kaskel, Improved synthesis, thermal stability and catalytic properties of the metal-organic framework compound Cu3(BTC)2, Microporous Mesoporous Mater. 73 (1) (2004) 81–88, https://doi.org/10.1016/j.micromeso.2003.12.027.

[31] I.L. Camargo, M.M. de; Morais, C.A. Fortulan, M.C. Branciforti, A review on the rheological behavior and formulations of ceramic suspensions for vat photopolymerization, Ceram. Int. 47 (9) (2021) 11906–11921, https://doi.org/10.1016/j.ceramint.2021.01.031.

[32] M. Thommes, K. Kaneko, A.V. Neimark, J.P. Olivier, F. Rodriguez-Reinoso, J. Rouquerol, K.S.W. Sing, Physisorption of gases, with special reference to the evaluation of surface area and pore size distribution (IUPAC Technical Report), Pure Appl. Chem. 87 (9–10) (2015) 1051–1069, https://doi.org/10.1515/pac-2014-1117.

[33] A. Bertero, J. Schmitt, H. Kaper, B. Coppola, P. Palmero, J.-M. Tulliani, MOFs functionalization of 3D printed mullite complex architectures for CO_2 capture, Appl. Mater. Today 40 (2024) 102407, https://doi.org/10.1016/j.apmt.2024.102407.

[34] J.E. Mondloch, O. Karagiaridi, O.K. Farha, J.T. Hupp, Activation of metal–organic framework materials, CrystEngComm 15 (45) (2013) 9258–9264, https://doi.org/10.1039/C3CE41232F.

[35] K. Sumida, D.L. Rogow, J.A. Mason, T.M. McDonald, E.D. Bloch, Z.R. Herm, T.-H. Bae, J.R. Long, Carbon dioxide capture in metal–organic frameworks, Chem. Rev. 112 (2) (2012) 724–781, https://doi.org/10.1021/cr2003272.

[36] S.-M. Hong, E. Jang, A.D. Dysart, V.G. Pol, K.B. Lee, CO_2 capture in the sustainable wheat-derived activated microporous carbon compartments, Sci. Rep. 6 (1) (2016) 34590, https://doi.org/10.1038/srep34590.

[37] S. Sircar, Excess properties and thermodynamics of multicomponent gas adsorption, J. Chem. Soc. Faraday Trans. 1 81 (7) (1985) 1527–1540, https://doi.org/10.1039/F19858101527.

[38] J. Moellmer, A. Moeller, F. Dreisbach, R. Glaeser, R. Staudt, High pressure adsorption of hydrogen, nitrogen, carbon dioxide and methane on the metal–organic framework HKUST-1, Microporous Mesoporous Mater. 138 (1) (2011) 140–148, https://doi.org/10.1016/j.micromeso.2010.09.013.

[39] C. Chen, B. Li, L. Zhou, Z. Xia, N. Feng, J. Ding, L. Wang, H. Wan, G. Guan, Synthesis of hierarchically structured hybrid materials by controlled self-assembly of metal–organic framework with mesoporous silica for CO_2 adsorption, ACS Appl. Mater. Interfaces 9 (27) (2017) 23060–23071, https://doi.org/10.1021/acsami.7b08117.

[40] B. Coasne, A. Galarneau, F. Di Renzo, R.J.M. Pellenq, Effect of morphological defects on gas adsorption in nanoporous silicas, J. Phys. Chem. C. 111 (43) (2007) 15759–15770, https://doi.org/10.1021/jp073678a.